Electron and Proton Conducting Framework Organic Salts Single Crystals

Guolong Xing,[a, c] Tingting Yan, [a, c] Steven Bailey, [b] Colin Lambert, [b] Pierre Fayon, [b] Abbie Trewin,*, [b]

and Teng Ben*, [a]

Organic molecular assemblies that can conduct both electrons and protons are attractive materials as they have important applications. Here we show the synthesis and characterization of two three-dimensional conducting framework organic salt (CFOS) single crystals that can both conduct electrons and protons, one of which is the first example of a salt organic network that contains a 3D super stacked π-conjugated network. We show that the resulting self-assembled crystalline structure can direct the CFOS to optimized electron or proton conduction through the change of a single carbon atom to a silicon atom, highlighting the potential for targeted design through fine control of the self-assembly process. Furthermore, the electron and proton conduction properties of the CFOS materials are highly dependent upon the crystallographic direction and are examples of purely organic anisotropic conductors. We find that electronic conduction occurs through the 3D super stacked π-conjugated network pathways whereas the proton conduction occurs via a novel combination of Grotthus and vehicular diffusion.

Introduction

Materials formed from organic networks are essential components of devices with varied applications, including as organic electronics and fuel cells.[1, 2] Conducting framework organic salts (CFOSs) constructed through non-covalent interactions such as π-π interactions and salt bridges (including hydrogen bonding and electrostatic interactions) are a new and interesting subset of these materials.[3] They are structurally diverse leading to great potential for a wide range of properties. They also have structural flexibility that can lead to unique properties such as dynamic and responsive guest uptake behaviors.[4a] This structural responsiveness facilitates the use of materials for applications such as sensors and memory devices.[4b]

Charge transport, whether electronic or proton, in purely organic materials such as conjugated polymers relies upon chemical functionality, including π-conjugation or acidic functionality, to create extended charge transport mechanisms.[5] However these advanced organic materials are increasingly complex and their multi-step synthesis is often costly.[5]

Organic salts have shown semiconducting[6a] and proton conducting properties[6b], but are more commonly found to contain metal ions.[7] The electrical conductivity of these materials arises from a combination of a small gap (<1.5 eV) between the highest occupied molecular orbital (HOMO) and lowest unoccupied molecular orbital (LUMO) and strong π-conjugation[8a] through a network, that can arise from direct covalent bonding or through π-π stacking between molecular units of different nets. Proton conduction occurs via two distinct design strategies, either by incorporation of water molecules within pore structure that can act as a charge carrier using a vehicular mechanism, or by inclusion of proton transfer agents such as acidic functionality that can transport protons via a Grotthus mechanism.[8b]

A challenge for materials scientists is to combine the ability to conduct protons and electrons into the same material as these properties often have competing structural requirements, for example void space to allow proton diffusion vs dense networks to allow efficient conduction of electrons. The design principle that we have taken here is to include phenyl-ring moieties that enable π-π stacking, and therefore potential electron conduction routes, combined with hydrogen bonding motifs in a 3D tecton to direct inefficient packing, and thereby introducing void space within which proton diffusion may occur. Here, we presented two CFOS materials that were based around a central 3-D tecton, CFOS-1 and CFOS-2 that were electronic and proton conducting. The CFOS materials were generated via self-assembly of the molecular tectons, shown in
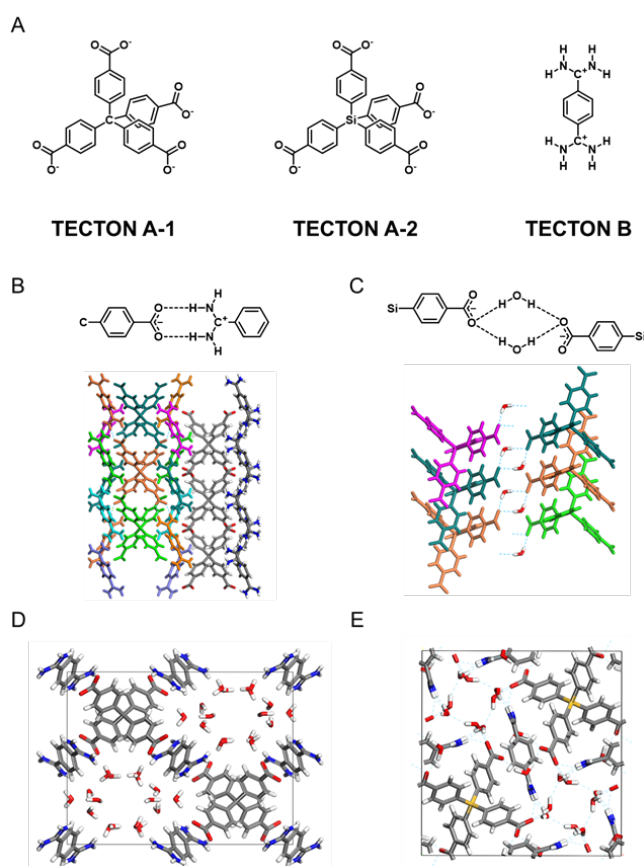

Figure 1. (A) Tecton A-1 (CFOS-1), A-2 (CFOS-2) and Tecton B. (B) Amidine/carboxylate eight-member ring-system synthon, R_2^2 in CFOS-1 and respective node-to node bonding. (C) Amidine/carboxylate/water synthon in CFOS-2 and respective node-to node bonding. (D) Crystal structure for CFOS-1. (E) Crystal structure for CFOS-2.

Figure 1A, by simple drop-wise addition and crystallization to form white needle like crystals. This simple and robust process provided a cheap, scalable and highly processable method of synthesis. The crystals synthesized were large enough for single crystal electron conductivity measurement by DC impedance spectra and proton conductivity measurement by AC impedance spectra.

Results and Discussion

Synthesis and Characterization. For the CFOS systems we used a tetrahedron-based unit, (Tecton A) combined with a linking bridge, which in both cases was terephthalimidamide (Tecton B). For CFOS-1 tetrakis(4-carboxyphenyl)methane (Tecton A-1) was used, and for CFOS-2 tetrakis(4-carboxyphenyl)silane (Tecton A-2) was used. The full synthetic procedure was outlined in Materials and Methods section of the supporting information. The crystal structures were resolved by single crystal X-ray diffraction and shown in Figure 1. For the crystal structures formed, two distinct forms of network bonding were observed (Figure 2): (i) π-π stacking and (ii) charge-assisted H-bonding. For CFOS-1, a diamondoid network was formed through charge-assisted hydrogen bonding between Tecton A-1 and B, forming an eight-member ring-system synthon, $R_2^2(8)$, shown in Figure 1B. This linking synthon has been utilized for other super molecular assembled network materials.[4b, 9] The crystal structure was formed through a ten-fold network interpenetration of the diamondoid nets, shown in Figure 1D and S8. Alternate π-π stacking between the phenyl rings of each Tecton A-1 and Tecton B leaded to a 3-D super stacked π-conjugated network between the interpenetrated nets. As shown in Figure 1C, 1E and S9, for CFOS-2, a diamondoid net was formed through charge-assisted hydrogen bonding of two linking water molecules between Tecton A-2s. Tecton B occupied space between the diamondoid net to fill space efficiently and maximize the electrostatic and π-π stacking interactions. A similar π-π stacking motif to CFOS-1 was found with π-π stacking of the phenyl rings of each Tecton A-2 and Tecton B (Figure S9).

In CFOS-1, Tecton A-1 forms charge assisted H-bonds directly with Tecton B. Whereas in CFOS-2, the H-bonded network from Tecton A-2 to Tecton B is mediated by charge assisted H-bonding to water molecules, with the two hydrogen atoms in the water H-bonded to Tecton A-2 and Tecton B respectively. The only atomic difference between Tecton A-1 and Tecton A-2 is that the central carbon is replaced by a silicon atom. To assess the difference that this change makes, DFT calculations of the respective tecton ion structures were undertaken. Tecton A-2 is slightly bigger than Tecton A-1 with the node to oxygen distance being 6.99 Å and 6.52 Å respectively. This is due to the increased size of the silicon atom and the resultant larger C-Si bond. Mulliken charge distribution, determined during the DFT calculations of the structure, provides information about the transfer of electronic charge between atoms and the charge distribution within the tecton.[10] The Mulliken charge assignments show that the carbon node has a greater positive charge at 2.496 than the silicon node at 2.016. Further differences can be seen in the charge distribution within the carboxylate groups. In Tecton A-1 the charge is spread equally with each oxygen atom having a charge of -0.516. Whereas in Tecton A-2, one oxygen within each carboxylate group has a charge of -0.516 and the other has a charge of -0.521. This results in the carboxylate groups of CFOS-2 being slightly more negative with a charge of -1.037 compared to the carboxylate charge of -1.032 in CFOS-1. Whilst these differences are very small, they can have a profound difference on the balance of packing efficiency and charge interactions in a crystalline salt structure.

A

Node-to-node through π-π stacking   Node-to-node through H-bonding

B

Node-to-node through π-π stacking   Node-to-node through H-bonding

Figure 2. The network bonding units for the CFOS series of materials. (A) CFOS-1. (B) CFOS-2.

A 1-D void channel filled with water molecules can be observed in both CFOS-1 and CFOS-2 (Figure 1D and 1E). For CFOS-1, the 1-D void channel was formed along the c-axis direction of the CFOS-1 cell. The occupying water molecules formed a hydrogen bonded $5^4 6^6$ polyhedra cage, shown in Figure S10. Hydrogen atoms of the water molecules either point along the vertices or out towards the CFOS-1 framework. The hydrogen atoms pointing along the vertices can occupy positions that point to either neighboring oxygen atoms equally with 50:50 occupation of each possible position. The Bernal-Fowler ice rules provides a set of principles to describe the arrangement of the water atoms and molecules to form the networked crystal structure of ice. It states that each oxygen atom in a water molecule must be covalently bonded to two hydrogen atoms and hydrogen bonded to two further hydrogen atoms, meaning that there is one hydrogen atom between every oxygen atom linking the water molecules together to form the ice structure.[11] Following these rules, the hydrogen atom configuration can be rationalized to form the $5^4 6^6$ polyhedra cage with hydrogen atoms in either configuration. The water cage is similar in dimension and shape to common clathrate hydrate
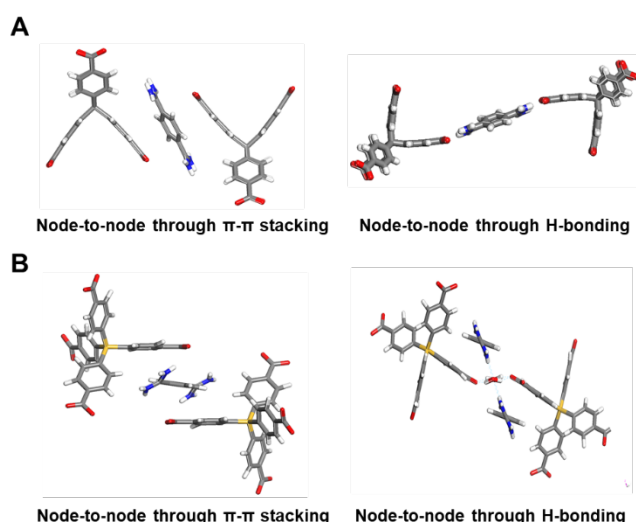
cages.[12] The water molecules at the center of the cage were hydrogen bonded to adjacent carboxylate oxygen. The upper and lower 6-membered rings of the cage were pinned within the 1-D channel by additional hydrogen bonded water molecules that were hydrogen bonded to the CFOS-1 network carboxylate groups in an *anti* position to the $R_2^2(8)$ ring.[9c] These pinning and cage water molecules occupied two positions equally – a position pointing upwards, and therefore the lower part of a cage above, or downwards, and therefore the upper part of a cage below. Occupying either position resulted in formation of a partial respective alternative cage. It is not possible to rationalize the structure without this partial cage formation. We therefore suggest that these pinning and cage water molecules alternate between these upper and lower positions resulting in transient cage – partial cage formation. For CFOS-2, the 1-D void channel was formed in the c-axis direction. Water molecules were localized at the edge of the 1-D channel with each water molecule being hydrogen bonded to adjacent carboxylic acid and amidine groups of Tecton A-2 and Tecton B. Further water molecules were hydrogen bonded to either a Tecton A-2 or a Tecton B.

To assess the relative void space that the water molecules occupy in each system, the theoretical surface areas of the COFSs were determined after removing the water molecules in the frameworks by using a probe radius of 1.82 Å. CFOS-1 has a calculated Connolly surface area of 2065 m^2 g^{-1}, while the Connolly surface area of CFOS-2 is calculated to be 1044 m^2 g^{-1}. The surface area of CFOS-1 is larger than for CFOS-2, reflecting the larger void volume that CFOS-1 has in order to accommodate the greater number of water molecules, 25.97 wt% compared to 20.51 wt% for CFOS-1 and CFOS-2.

For CFOS-1 and CFOS-2, thermogravimetric analysis (TGA) showed 11.2 wt.% and 11.7 wt.% loss in mass between 50 and 150°C respectively, shown in Figure S2. This did not match the crystallographically determined water content of 25.97 wt.% and 20.51 wt.% for CFOS-1 and CFOS-2 respectively. We can assign the remaining water mass to water molecules that were bound directly to the CFOS framework (circled in green in Figure S11). A further decrease in mass at 245°C (24.7 wt.%) and 232°C (19.1 wt.%) for CFOS-1 and CFOS-2 respectively can be assigned to the loss of these more strongly bound water molecules.

The morphology of CFOSs were expolred by optical microscope. Both of the CFOSs had a needle like morphology (Figure S4). The large single crystals of CFOSs were picked up for the mesurement and the size of cross-section of CFOS-1 and CFOS-2 were of 29 × 32 μm and 18 × 17 μm, respectively.

Electron conduction of CFOSs (single crystal). Measurements of electrical conductance data were presented in Figure 3 and summarized in Table S2. For CFOS-1, an electrical resistivity, ρ = 2.03 x 10³ Ω cm (333 K) was found only along the crystal c-axis, giving a conductance, σ = 4.93 x 10⁻⁴ S cm⁻¹ (333 K). No conductance was observed along the a- and b- axes. For CFOS-2 a larger electrical resistivity of ρ = 1.60 x 10⁴ Ω cm (323 K) was found giving a conductance of σ = 6.25 x 10⁻⁵ S cm⁻¹ (323 K). In Figure 3, the I/V plots of CFOS-1 and CFOS-2 were compared as a function of temperature between 273 and 373 K. CFOS-1 and CFOS-2 exhibited semiconductor like conductivity dependence with temperature shown in Figure 3C. A similar resistivity and conductance was found for a self-assembly of an acid functionalised tetraphenylethylene derivative and a bis(pyridine), **1.BPE,** of ρ = 3.6 Ω cm and σ = 0.28 S cm⁻¹.[6a] Since typical conductivities of purely organic semiconducting materials are σ ≈ 10⁻⁶ S cm⁻¹, these values are comparable with the best established purely organic semiconductors,[13] including non-doped polyacene and thiophene based organic semiconductors.[6a]

Computation for electron conduction. To rationalize the conduction properties of CFOS-1 and CFOS-2, ab-initio calculations were performed using the SIESTA[14] implementation of density functional theory (DFT) (see part 9 in SI for details). The total energy of each system was minimized by fully relaxing the unit cell and from this lowest-energy state we computed the total electronic density of states (DOS) and partial density of states (PDOS) for each atomic species of the CFOS-1 crystal structure. The DOS (g(E)dE) is the number of one-electron levels between energies E and dE whereas the PDOS (g(u, E)dE) is the number of one-electron levels with weight on a defined orbital u between energies E and dE. These are related by $g(E) = \sum_u g(u, E)$). The results were shown in Figure S12, which reveals that for CFOS-1, the PDOS for carbon dominated and the LUMO peak at ~2.3 eV was a combination of nitrogen and carbon states, whereas the LUMO+1 peak at ~2.5 eV was due to carbon and oxygen. Furthermore the LUMO+2 had three peaks between 3.0 and 4.0 eV, where the first peak was composed of carbon and oxygen states, the second of carbon and the third of carbon and nitrogen. The HOMO at ~ -0.75 eV was dominated by carbon orbitals. These results suggested that the conduction pathway is primarily due to π-π stacking. The finite widths of the mini-bands associated with the HOMO-1 and LUMO+2 peaks indicated that they mediate electronic conductance in those directions, whereas in the x and the y direction the mini-bands were very nearly flat indicating that in these directions there will be negligible electron transport (Figure
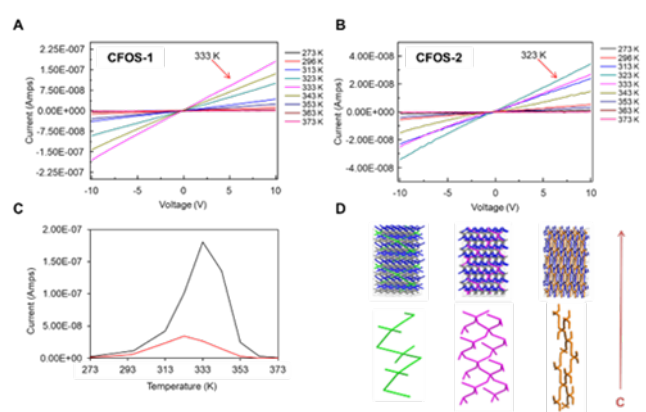

Figure 3. (A) Current/Voltage plot for a range of temperatures for CFOS-1. **(B)** Current/Voltage plot for a range of temperatures for CFOS-2. **(C)** Current/Temperature plot for CFOS-1 (black) and CFOS-2 (red). **(D)** Conduction pathways available in the C crystallographic direction: Green pathway following the charge assisted H-bonds; Pink pathway following alternate charge assisted H-bonds and π-stacking; and Orange pathway following π-stacking.

S13). Figure S14 showed that the HOMO-1 to LUMO band gap is 2.82 eV for CFOS-1, there is a mini-gap between the LUMO and LUMO+1 of 0.25 eV and a mini-gap between the LUMO+1 and LUMO+2 of 0.42 eV.

Assessment of the CFOS-1 crystal structure revealed three potential pathways within the cell. These correspond to (i) Green pathway – Tecton A-1 and Tecton B linked directly through the charge assisted hydrogen bonds, (ii) Orange pathway – Tecton A-1 and Tecton B linked via π- π stacking, and (iii) Pink pathway – Tecton A-1 and Tecton B linked through combination of charge assisted hydrogen bonding and π- π stacking. The pathways are shown in Figure 3D. To reinforce the theoretical prediction of the existence of conductance pathways demonstrated by the finite bandwidth of mini bands, the real part of the electronic wavefunctions can be represented as isosurfaces mapped onto the atomic sites. The isosurfaces of the HOMO-1 was dominated by Tecton A-1, the LUMO by Tecton B, and the LUMO+1 by Tecton A-1. None of these demonstrated a viable pathway either through π-π stacking or hydrogen bonding. The isosurface of the LUMO+2 was a combination of Tecton A-1 and Tecton B and was shown in Figure S15. The electron density in Figure S15 added to the evidence for conduction through the orange π-π stacking path.

These calculations showed large differences in the band gap for each of the respective pathways available, which rationalized the experimentally measured dependence of electronic conduction on the orientation of the crystal. Clearly as water is an integral component of the crystal structure there is no necessity to dry the sample. It should be noted that for the entire family of porous materials, π-conjugated networks are always found in 2D systems like 2D-MOFs, 2D-COFs, 2D-CMPs, etc., CFOS-1 provides a unique organic salt network of 3D super stacked π-conjugated network, combining an interesting semi-conductivity with a 3D network.

For CFOS-2, a similar pathway to the orange pathway was found within the crystal structure with a similar π-π stacking motif between Tecton A-2 and Tecton B. For CFOS-2, the distance between the phenyl rings of the π-π stacks was slightly larger at 4.29 Å compared to 4.25 Å for CFOS-1. Also, Tecton B in CFOS-2 was rotated by approximately 45° compared to Tecton B in CFOS-1 (Figure S7). Furthermore, Figure S14 showed that the HOMO to LUMO band gap is 3.30 eV for CFOS-2 which is larger than that of CFOS-1. Therefore, combined with the larger π-π stacking distance, this rationalizes the lower conductivity observed for CFOS-2.

The plot of current versus temperature for CFOS-1 and CFOS-2, Figure 3C, showed that a maximum in the current occurs at 333 K for CFOS-1 and at 323 K for CFOS-2. This is consistent with semi-conducting behavior, where promotion of electrons from the HOMO to the LUMO levels increases with temperature. We suggested that the decrease in current at higher temperature is due to thermal motion of the network, which reduces the connectivity and overlap of the connecting π-π stacks. To assess the influence of temperature on the distance between the π-π-stacked phenyl rings and charge-assisted hydrogen bonds, we ran Carr Parinello molecular dynamic simulations (CPMD) at 298 K and at 398 K for CFOS-1. The pair distribution function (PDF) for C-C of the π-π stacking phenyl rings in Tecton A-1 and Tecton B were calculated for each temperature, shown in Figure S16. We saw that at higher temperatures, the PDF was expanded to include larger distances showing that the distances with the maximum distance measured increasing from 4.4 Å to 4.5 Å. Small increases in the π-π stacking distance will dramatically reduce the orbital overlap and hence connectivity of the electron conduction pathway.

Proton conduction of CFOSs (powder). The polar channels of CFOSs and the water molecules in the channels facilitate proton conduction which motive us to explore the proton conduction performance of CFOSs. The proton conductivity of the crystalline powder sample was measured by electrochemical impedance
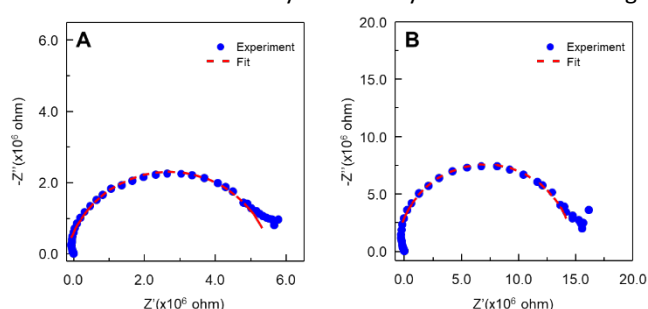

Figure 4. Nyquist plots and fitted curves of single crystals of (**A**) CFOS-1 and (**B**) CFOS-2.
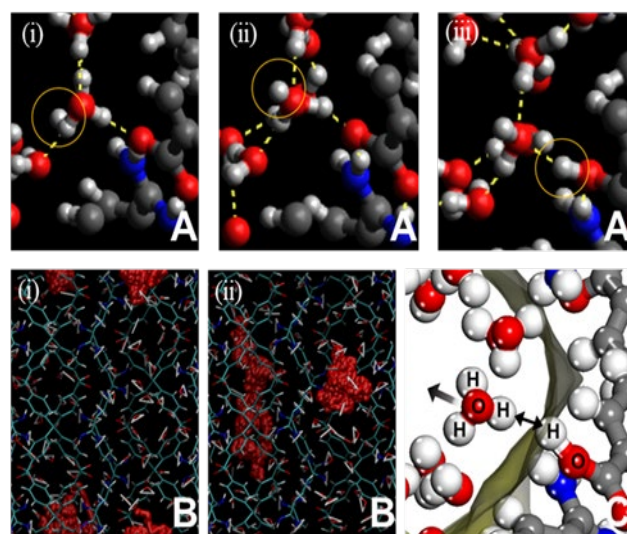

Figure 5. (A) Proton transfer in CFOS-1 via the Grotthus mechanism: (i) the proton starts as part of a hydronium ion, (ii) a neighbouring water molecule is protonated to form a new hydronium ion, (iii) a neighbouring carboxylate group is protonated to form a carboxylic acid group. **(B)** Trajectory showing proton diffusion via a vehicular mechanism: (i) the hydronium ions (the hydronium oxygen trajectory is shown in red) are limited to one water cage (ii) the dynamic motion of nearby water molecules allows the hydronium ions to pass into adjacent water cages where they are limited to until the next water cage becomes accessible. **(C)** Overall diffusion mechanism scheme for CFOS-1 and CFOS-2. The proton is in a dynamic equilibrium between channel water molecules as a hydronium ion and the Tecton A carboxylate groups as a hydroxyl group. Proton diffusion occurs via a vehicular mechanism when the proton is part of a hydronium ion.

spectroscopy (EIS) in the form of pellets. Time-dependent proton conductivity measurements were performed to investigate the influence of time on proton conduction. [15-17] The proton conductivity of CFOSs gradually increased with the increase of time which can be attributed to the increased water concentration. It is demonstrated that the concentration of proton carrier plays a vital role on proton conductivity.[18] After 24 h, the proton conductivity of CFOSs slightly increased indicating that water sorption almost reached an equilibrium until a maximum was reached at 48 h (Figure S17 and S18). Temperature-dependent proton conductivity measurements were performed from 298 K to 323 K under high humidity conditions. Typical Nyquist plots with semi-circle in the high-frequency region and tail in the low-frequency region were observed (Figure S19 and S20). At 298 K and 98% RH, the proton conductivities of CFOS-1 (powder sample) and CFOS-2 (powder sample) were found to be 2.6×10^{-6} S cm^{-1} and 4.4×10^{-6} S cm^{-1}, respectively. With the increase of temperature, the resistance of CFOSs were decreased. When the temperature was evaluated to 323 K, the proton conductivities reached to 1.9×10^{-4} S cm^{-1} and 2.2×10^{-4} S cm^{-1} for CFOS-1 and CFOS-2, which are moderate values in crystalline organic materials. Under anhydrous condition, CFOSs did not exhibit obvious proton conduction behavior which demonstrated the importance of water molecules in proton conduction (Figure S23 and S24). After the EIS measurements, the PXRD patterns of CFOSs powders showed no significant changes which indicated that the structure of the CFOSs were still retained (Figure S25 and S26). Intriguingly, as shown in Figure S25, partial CFOS-1 exhibited amorphous after grinding which can be attributed to the losing of water molecules in the channels. During the EIS measurement under high humidity, the crystallinity of CFOS-1 could be recovered by adsorbing water molecules. Therefore, CFOS-1 showed a better PXRD pattern after EIS measurement.

Proton conduction of CFOSs (single crystal). The anisotropy of electron conduction inspired us to explore the proton conduction performance of CFOSs in the form of single crystals. To gain insight of the proton conduction behavior in different direction, single-crystal conductivity measurements were performed at 298 K and 98% RH. Interestingly, at 298 K and 98% RH, the proton conductivities of the single crystals of CFOS-1 and CFOS-2 can reach as high as 1.4×10^{-2} S cm^{-1} and 8.6×10^{-3} S cm^{-1}, Figure 4, which are four orders of magnitude higher than CFOS-1 measured with pellet and three orders of magnitude higher than CFOS-2 measured with pellet at the same condition. It can be attributed to the disappearance of the grain boundary resistance and the effective proton transport along the channels. These values are comparable to the highest proton conductivity reported to date, if not greater than the values of single crystals, e. g. [Zn(H$_2$PO$_4$)$_2$(TzH)$_2$](1.1×10^{-4} S cm^{-1}, 403 K, 0% RH),[19] CPM-102(1.1×10^{-2} S cm^{-1}, 295.5 K, 98.5% RH),[20] CB[6]·1.1 HCl·11.3H$_2$O(2.4×10^{-2} S cm^{-1}, 298 K, 98% RH),[21] and also comparable to the values reported for some crystalline organic materials measured with pellets including CPOS-2 (2.2×10^{-2} S cm^{-1}, 333 K, 98% RH),[15] HOF-GS-11 (1.8×10^{-2} S cm^{-1}, 303 K, 95% RH),[22] Im@Fe-MOF (1.21×10^{-2} S cm^{-1}, 333 K, 98% RH).[23]The proton transport mechanism within CFOS-1 and CFOS-2 is an interesting question. According to temperature-dependent proton conductivity measurements, the Arrhenius plots of CFOSs were obtained and linearly approximated well (Figure S21 and S22). The activation energy (E_a) was estimated as 1.60 eV and 1.36 eV for CFOS-1 and CFOS-2, respectively. These values are higher than 0.4 eV, which is typically associated with a vehicular conduction mechanism. This implies that the proton transport occurs with water molecules as carriers rather than via the Grotthus mechanism. Assessing the structure of the water molecules within the CFOS-1 and CFOS-2 structure, there is a well-defined hydrogen-bonded network and so it is not clear why the Grotthus mechanism is not adopted. Furthermore, Figure S27A showed the Connolly surface of CFOS-1 with non-connected voids when the channel water is present. A fully connected void space was available with the channel water removed. For CFOS-2, no Connolly surface was available if the channels were filled with water, but a connected void space was available when the channel water was removed. (Figure S27B). This indicated that direct vehicular diffusion of a hydronium ion would not be possible.

Computation for proton conduction. To assess the proton diffusion further we ran Carr Parinello molecular dynamic simulations (CPMD) of the CFOS-1 system with one water molecule in the water cage protonated to give a hydronium ion. The system quickly rearranged so that a neighboring water molecule was protonated and then again so that an oxygen of the carboxylate was protonated. This rearrangement occured via a typical Grotthuss mechanism (Figure 5A). The same result occured if two water molecules in neighboring channels were protonated. However, if two water molecules in the same channel were protonated then the crystal structure broke down after two carboxylate groups were protonated. This suggested that proton diffusion via the Grotthuss mechanism is possible but that the protons are rapidly bound to the carboxylate groups. It is possible that the increased activation energy is due to having to remove the protons from the carboxylate groups leading to a high barrier Grotthuss mechanism. The energetic barrier to removing a proton from the carboxylate of Tecton A-1 and Tecton A-2 was determined using DFT, shown in Figure S29. In both cases, an energetic barrier of ~0.45 eV was determined, within the expected values for a Grotthuss type transfer mechanism. However, for both CFOS-1 and CFOS-2 it is energetically favorable by ~0.05 eV for the proton to exist within a carboxylic acid group than within a hydronium ion. We therefore concluded that the carboxylate acts as a sink for proton transfer via the Grotthuss mechanism, preventing direct diffusion along the channel via this mechanism.

To assess the potential for vehicular diffusion, the diffusion of a proton via a hydronium ion was determined using classical molecular dynamics. For CFOS-1 and CFOS-2, one water molecule in each channel was protonated and its diffusion monitored for the duration of the simulation. For CFOS-1 we saw that the hydronium ion remained in the non-connected void for 0.02 ns and then was able to move into a neighboring void, shown in Figure 5B. There were five water molecules that were situated at the top of the water cage that in the static crystal structure block the connection of the voids within each water cage. Figure S30 showed

that these water molecules were able to move from their crystal positions and that the hydronium ion was able to take advantage of a brief moment when the water molecules were far enough apart that the cage voids become connected and the hydronium can pass through to the neighboring cage. Whereas the hydronium in the CFOS-2 system was able to steadily diffuse along the channel, enabled by the diffusion of the adjacent water molecules of the channel, shown in Figure S31. As the vehicular diffusion of the hydronium ion in each case is dependent upon the motion of adjacent water molecules, we expect that as the temperature is increased the water molecules will have increased motion and therefore the hydronium ions will be able to diffuse more easily. We can therefore concluded that proton diffusion occurs via two mechanisms: (i) the Grotthuss mechanism where the proton is in an equilibrium between the carboxylate and the channel water, and (ii) vehicular diffusion that occurs when the proton is in a channel hydronium, shown in Figure 5C. This finding contradicts the common belief that 0.4 ev is not a threshold to determine the mechanism of proton conductivity. Overall diffusion towards an anode occurs via the vehicular diffusion and is dependent upon the motion of the other channel water molecules. At low temperature, the water molecules do not move enough to allow the hydronium ions to diffuse. As the temperature is increased, the motion of these water molecules increases and thus allows diffusion of the hydronium ion by a vehicular mechanism. We postulate that as CFOS-2 has fewer water molecules within its void space compared to CFOS-1, the temperature at which diffusion of the water molecules allows hydronium ion diffusion is lower and therefore the activation energy is lower.

It is worth noting that CFOS-1 has an optimized charge transport compared to CFOS-2. These differences are a direct result of the respective crystal structures of CFOS-1 and CFOS-2 which in turn are a direct result of the change in chemical structure of Tecton A-1 and A-2. Tecton A-1 (CFOS-1) has a carbon core whereas Tecton A-2 has a silicon core. This small chemical change has a dramatic effect on the resulting self-assembled crystal structures. This indicates that there is great potential for further tailoring of the resultant properties by exploring the chemical diversity that is available.

Conclusions

In conclusion, we have synthesized a new series of conducting framework organic salt materials, which exhibit electron conductivity and proton conductivity. Electron and proton conductivity of CFOSs are controlled by a minor change of one atom in the tecton build units. This change directs the packing and thereby controls the self-assembled crystal structure and hence directing the electron and proton conduction properties. This opens up the potential for the discovery of new conducting organic materials with tunable structures for specific applications realized through fine control of the self-assembled crystal structure.

Conflicts of interest

There are no conflicts to declare.

Acknowledgements

Notes and references

1   S. Das, P. Heasman, T. Ben and S. Qiu, *Chem. Rev.* 2017, **117**, 1515.
2   S. Chand, S. C. Pal, A. Pal, Y. Ye, Q. Lin, Z. Zhang, S. Xiang and M. C. Das, *Chem. –Eur. J.* 2019, **25**, 1691.
3   (a) N. G. White, *Dalton Trans.* 2019, **48**, 7062; (b) Y. Zhao, C. Fan, C. Pei, X. Geng, G. Xing, T. Ben and S. Qiu, *J. Am. Chem. Soc.* 2020, 10.1021/jacs.9b13274; (c) G. Xing, I. Bassanetti, T. Ben, S. Bracco, P. Sozzani, L. Marchiò and A. Comotti, *Cryst. Growth Des.* 2018, **18**, 2082; (d) G. Xing, I. Bassanetti, S. Bracco, M. Negroni, C. Bezuidenhout, T. Ben, P. Sozzani and A. Comotti, *Chem. Sci.* 2019, **10**, 730.
4   (a) D. Holden, K. E. Jelfs, A. Trewin, D. J. Willock, M. Haranczyk, and A. I. Cooper, *J. Phys. Chem. C* 2014, **118**, 12734; (b) A. Yamamoto, T. Hasegawa, T. Hamada, T. Hirukawa, I. Hisaki, M. Miyata, and N. Tohnai, *Chem. –Eur. J.* 2013, **19**, 3006.
5   S. R. Forrest, *Nature* 2004, **428**, 911.
6   (a) P. P. Kapadia, L. R. Ditzler, J. Baltrusaitis, D. C. Swenson, A. V. Tivanski, and F. C. Pigge, *J. Am. Chem. Soc.* 2011, **133**, 8490; (b) M. Yamada and I. Honma, *Electrochim. Acta* 2003, **48**, 2411.

7   (a) M. G. Miles and J. D. Wilson, *Inorg. Chem.* 1975, **14**, 2357; (b) S. Kim, B. Joarder, J. A. Hurd, J. Zhang, K. W. Dawson, B. S. Gelfand, N. E. Wong and G. K. H. Shimizu, *J. Am. Chem. Soc.* 2018, **140**, 1077.

8   (a) D. Hong, M. Lv, M. Lei, Y. Chen, P. Lu, Y. Wang, J. Zhu, H. Wang, M. Gao, S. E. Watkins, and X. Chen, *ACS Appl. Mater. Interfaces* 2013, **5**, 10995; (b) H. Xu, S. Tao and D. Jiang, *Nat. Mater.* 2016, **15**, 722.

9   (a) W. Wei, W. Li, X. Wang and J. He, *Cryst. Growth Des.* 2013, **13**, 3843; (b) S. Lie, T. Maris and J. D. Wuest, *Cryst. Growth Des.* 2014, **14**, 3658; (c) V. N. Yadav and C. H. Gorbitz, *CrystEngComm* 2013, 15, 439; (d) L. Pop, N. D. Hadade, A. van der Lee, M. Barboiu, I. Grosu and Y.-M. Legrand, *Cryst. Growth Des.* 2016, **16**, 3271.

10 R. S. Mulliken, *J. Chem. Phys.* 1955, **23**, 1833.

11 J. D. Bernal and R. H. Fowler, *J. Chem. Phys.* 1933, **1**, 515.

12 (a) P. S. R. Prasad, T. Sugahara, A. K. Sum, E. D. Sloan and C. A. Koh, *J. Phys. Chem. A* 2009, **113**, 6540; (b) J. Zhu, S. Du, X. Yu, J. Zhang, H. Xu, S. C. Vogel, T. C. Germann, J. S. Francisco, F. Izumi, K. Momma, Y. Kawamura, C. Jin and Y. Zhao, *Nat. Commun.* 2014, **5**, 4128.

13 A. G. MacDiarmid, *Synth. Met.* 2001, **125**, 11.

14 M. S. José, A. Emilio, D. G. Julian, G. Alberto, J. Javier, O. Pablo and S.-P. Daniel, *J. Phys. –Condens. Mat.* 2002, **14**, 2745.

15 G. Xing, T. Yan, S. Das, T, Ben and S. Qiu, *Angew. Chem. Int. Ed.* 2018, **57**, 5345.

16 M. Liu, L. Chen, S. Lewis, S. Y. Chong, M. A. Little, T. Hasell, I. M. Aldous, C. M. Brown, M. W. Smith, C. A. Morrison, L. J. Hardwick and A. I. Cooper, *Nat. Commun.* 2016, **7**, 12750

17 S. Chandra, T. Kundu, S. Kandambeth, R. Babarao, Y. Marathe, S. M. Kunjir and R. Banerjee, *J. Am. Chem. Soc.* 2014, **136**, 6570.

18 D. Umeyama, S. Horike, M. Inukai, Y. Hijikata and S. Kitagawa, *Angew. Chem. Int. Ed.* 2011, **50**, 11706.

19 D. Umeyama, S. Horike, M. Inukai, T. Itakura and S. Kitagawa, *J. Am. Chem. Soc.* 2012, **134**, 12780.

20 X. Zhao, C. Mao, X. Bu, P. Feng, *Chem. Mater.* 2014, **26**, 2492.

21 M. Yoon, K. Suh, H. Kim, Y. Kim, N. Selvapalam and K. Kim, *Angew. Chem. In. Ed.* 2011, **50**, 7870.

22 A. Karmakar, R. Illathvalappil, B. Anothumakkool, A. Sen, P. Samanta, A. V. Desai, S. Kurungot and S. K. Ghosh, *Angew Chem. Int. Ed.* 2016, **55**, 10667.

23 F.-M. Zhang, L.-Z. Dong, J.-S. Qin, W. Guan, J. Liu, S.-L. Li, M. Lu, Y.-Q. Lan, Z. M. Su and H.-C. Zhou, *J. Am. Chem. Soc.* 2017, **139**, 6183.